

# General-purpose machine-learned potential for 16 elemental metals and their alloys

Keke Song,<sup>1,\*</sup> Rui Zhao,<sup>2,\*</sup> Jiahui Liu,<sup>1</sup> Yanzhou Wang,<sup>3,1</sup> Eric Lindgren,<sup>4</sup> Yong Wang,<sup>5</sup> Shunda Chen,<sup>6</sup> Ke Xu,<sup>7</sup> Ting Liang,<sup>7</sup> Penghua Ying,<sup>8</sup> Nan Xu,<sup>9,10</sup> Zhiqiang Zhao,<sup>11</sup> Jiuyang Shi,<sup>5</sup> Junjie Wang,<sup>5</sup> Shuang Lyu,<sup>12</sup> Zezhu Zeng,<sup>12</sup> Shirong Liang,<sup>13</sup> Haikuan Dong,<sup>14</sup> Ligang Sun,<sup>13</sup> Yue Chen,<sup>12</sup> Zhuhua Zhang,<sup>11</sup> Wanlin Guo,<sup>11</sup> Ping Qian,<sup>1</sup> Jian Sun,<sup>5,†</sup> Paul Erhart,<sup>4,‡</sup> Tapio Ala-Nissila,<sup>3,15</sup> Yanjing Su,<sup>1,§</sup> and Zheyong Fan<sup>14,¶</sup>

<sup>1</sup>*Beijing Advanced Innovation Center for Materials Genome Engineering, University of Science and Technology Beijing, Beijing 100083, P. R. China*

<sup>2</sup>*School of Materials Science and Engineering, Hunan University, Changsha 410082, China*

<sup>3</sup>*MSP group, QTF Centre of Excellence, Department of Applied Physics, Aalto University, FI-00076 Aalto, Espoo, Finland*

<sup>4</sup>*Chalmers University of Technology, Department of Physics, 41926 Gothenburg, Sweden*

<sup>5</sup>*National Laboratory of Solid State Microstructures, School of Physics and Collaborative Innovation Center of Advanced Microstructures, Nanjing University, Nanjing 210093, P. R. China*

<sup>6</sup>*Department of Civil and Environmental Engineering, George Washington University, Washington, DC 20052, USA*

<sup>7</sup>*Department of Electronic Engineering and Materials Science and Technology Research Center, The Chinese University of Hong Kong, Shatin, N.T., Hong Kong SAR, 999077, P. R. China*

<sup>8</sup>*Department of Physical Chemistry, School of Chemistry, Tel Aviv University, Tel Aviv, 6997801, Israel*

<sup>9</sup>*Institute of Zhejiang University-Quzhou, Quzhou 324000, P. R. China*

<sup>10</sup>*College of Chemical and Biological Engineering, Zhejiang University, Hangzhou 310027, P. R. China*

<sup>11</sup>*State Key Laboratory of Mechanics and Control of Mechanical Structures, Key Laboratory for Intelligent Nano Materials and Devices of Ministry of Education,*

*and Institute for Frontier Science, Nanjing University of Aeronautics and Astronautics, Nanjing 210016, P. R. China*

<sup>12</sup>*Department of Mechanical Engineering, The University of Hong Kong, Pokfulam Road, Hong Kong SAR, P. R. China*

<sup>13</sup>*School of Science, Harbin Institute of Technology, Shenzhen, 518055, P. R. China*

<sup>14</sup>*College of Physical Science and Technology, Bohai University, Jinzhou 121013, P. R. China*

<sup>15</sup>*Interdisciplinary Centre for Mathematical Modelling, Department of Mathematical Sciences, Loughborough University, Loughborough, Leicestershire LE11 3TU, UK*

(Dated: November 12, 2023)

Machine-learned potentials (MLPs) trained against quantum-mechanical reference data have demonstrated remarkable accuracy, surpassing empirical potentials. However, the absence of readily available general-purpose MLPs encompassing a broad spectrum of elements and their alloys hampers the applications of MLPs in materials science. In this study, we present a feasible approach for constructing a unified general-purpose MLP for numerous elements and showcase its capability by developing a model (UNEP-v1) for 16 elemental metals (Ag, Al, Au, Cr, Cu, Mg, Mo, Ni, Pb, Pd, Pt, Ta, Ti, V, W, Zr) and their diverse alloys. To achieve a complete representation of the chemical space, we demonstrate that employing 16 one-component and 120 two-component systems suffices, thereby avoiding the enumeration of all 65 535 possible combinations for training data generation. Furthermore, we illustrate that systems with more components can be adequately represented as interpolation points in the descriptor space. Our unified MLP exhibits superior performance across various physical properties as compared to the embedded-atom method potential, while maintaining computational efficiency. It achieves a remarkable computational speed of  $1.5 \times 10^8$  atom step/s in molecular dynamics simulations using eight 80-gigabyte A100 graphics cards, enabling simulations up to 100 million atoms. We demonstrate the generality and high efficiency of the MLP in studying plasticity and primary radiation damage in the MoTaVW refractory high-entropy alloys, showcasing its potential in unraveling complex materials behavior. This work represents a significant leap towards the construction of a unified general-purpose MLP encompassing the periodic table, with profound implications for materials research and computational science.

Atomistic simulations of elemental metals and their alloys play a crucial role in understanding and engineering materials properties. While quantum-mechanical methods such as density-functional theory (DFT) calculations can be directly used for small simulation cells and short sampling times, their feasibility quickly diminishes with increasing spatial and temporal scales. For large-scale classical atomistic simulations, both molecular dynamics

(MD) and Monte Carlo (MC) simulations crucially depend on interatomic potentials. For metallic systems in particular, embedded-atom method (EAM)-type potentials [1, 2] have proven to be useful and been extensively applied over the past decades, especially for elemental metals and their alloys. However, these existing classical interatomic potentials often lack the required level of accuracy for numerous applications. This deficiency

primarily stems from constrained functional forms. Recently, a novel paradigm for developing interatomic potentials has emerged based on machine learning (ML) techniques [3–8]. In a machine-learned potential (MLP), the interatomic potential is modeled using ML methods, allowing for a significantly greater number of fitting parameters and providing versatility as compared to traditional many-body potentials. The functional forms of these MLPs are remarkably flexible, free from the limitations of a small number of analytical functions suggested by physical and chemical intuition or fitting to ground state properties only. The combination of flexible functional forms and a large number of fitting parameters empowers MLPs to achieve a level of accuracy that can be well beyond that of the traditional many-body potentials.

The basic theory behind MLPs is rather mature now. There are two main ingredients of a MLP: the regression model and the descriptors as inputs to the regression model. For the construction of input descriptors, linearly complete basis functions for the atom-environments have been proposed [9, 10]. For the regression model, linear regression [9, 11], artificial neural network (NN) regression [12], and kernel-based regression [13] are all proven to be feasible approaches. The combination of equivariant (as opposed to invariant) constructions and message passing or graph NN [14, 15] has also shown great potential in enhancing the regression accuracy of MLPs, albeit at the cost of reduced computational efficiency and challenges in maintaining parallelism.

Despite the higher accuracy offered by MLPs, they are still not as widely used in materials modeling. There are two main reasons for this, namely the relatively higher computational cost of the MLPs as compared to most of conventional many-body potentials, and the absence of a readily usable database of MLPs that covers a large number of elements and their compounds. In some cases where an extensive database is available, one can use an available MLP to study a specific problem, but in many cases, one has to train a new one or improve existing MLPs before being able to study the problem at hand. In particular, there is no simple way to combine MLPs for different elements to build MLPs for their compounds. This can lead to repeated efforts in the community and the case-by-case approach of developing MLPs is neither optimal nor sustainable in the long run. Regarding the computational cost of MLPs, the neuroevolution potential (NEP) approach [16–18] developed recently has been shown to yield excellent computational efficiency compared to other state-of-the-art methods, thanks to an optimization of the theoretical formalism and an efficient implementation in the GPUMD package [19]. The NEP approach can reach computational speeds unprecedented for MLPs on par with empirical potentials, paving the way for the application of MLPs to large-scale atomistic simulations.

In this paper, we introduce a sustainable approach for the construction of MLPs. Although our approach can be utilized to construct a comprehensive MLP covering the entire periodic table, we have chosen a more focused task as a proof of concept. Our objective is to develop a general-purpose NEP model encompassing 16 elemental metals and their alloys. Previous attempts to create general-purpose MLPs for numerous elements, or even the entire periodic table, have been initiated by researchers such as Takamoto *et al.* [20, 21] and Chen and Ong [22]. These studies have introduced “universal” MLPs, covering up to 45 elements [21] and 89 elements [22], respectively. Despite being termed universal, these MLPs have a rather limited application range and are orders of magnitude slower than EAM potentials. General-purpose MLPs have only been conclusively demonstrated for elemental matter such as Si [23], C [24], Fe [25], and Pb [26]. Here, our goal is to construct a genuinely general-purpose MLP for a diverse range of elements that matches the speed of EAM potentials and surpasses it in various physical properties.

Apart from achieving high accuracy and efficiency for the unified NEP model, which we term version 1 of unified NEP (UNEP-v1), we also propose an efficient approach to construct the training dataset. Constructing a training dataset with all the possible chemical compositions is a formidable task. Fortunately, the NEP descriptor parameters depend only on pairs of elements. We will demonstrate that considering unaries and binaries alone for the training dataset is sufficient, yielding a NEP model that is transferable to systems with more components. Using this route, we achieve a transferable NEP model for 16 elements using only about 70 000 reference structures. This accomplishment is demonstrated in large-scale MD simulations for mechanical deformation and primary radiation damage of high-entropy alloys.

## RESULTS

**A neural-network architecture for many-component systems.** Our starting point is the NEP approach as described in Ref. 18, called NEP3. In this work, we introduce two crucial extensions to NEP3 designed specifically for many-component systems. This extended approach will be called NEP4, which has been implemented in version 3.8 of GPUMD during the course of this work.

We first briefly introduce NEP3 [18], which is a NN potential [12] that maps a descriptor vector  $\mathbf{q}^i$  (with  $N_{\text{des}}$  components) of a central atom  $i$  to its site energy  $U_i$ . The total energy of a system of  $N$  atoms is expressed as the sum of the site energies  $U = \sum_{i=1}^N U_i$ . The ML model is a fully connected feedforward NN with a single hidden

layer with  $N_{\text{neu}}$  neurons:

$$U^i = \sum_{\mu=1}^{N_{\text{neu}}} w_{\mu}^{(1)} \tanh \left( \sum_{\nu=1}^{N_{\text{des}}} w_{\mu\nu}^{(0)} q_{\nu}^i - b_{\mu}^{(0)} \right) - b^{(1)}, \quad (1)$$

where  $\tanh(x)$  is the activation function in the hidden layer,  $\mathbf{w}^{(0)}$  is the connection weight matrix from the input layer (descriptor vector) to the hidden layer,  $\mathbf{w}^{(1)}$  is the connection weight vector from the hidden layer to the output layer,  $\mathbf{b}^{(0)}$  is the bias vector in the hidden layer, and  $b^{(1)}$  is the bias in the output layer. Denoting the weight and bias parameters in the NN collectively as  $\mathbf{w}$ , we can formally express the site energy as

$$U^i = \mathcal{N}(\mathbf{w}; \mathbf{q}^i). \quad (2)$$

The descriptor vector consists of a number of radial and angular components. For illustration, we here discuss the three-body angular components. Interested readers are referred to Ref. 18 for the description of higher-order terms. A three-body angular descriptor component can be expressed as

$$q_{nl}^i = \sum_{j \neq i} \sum_{k \neq i} g_n(r_{ij}) g_n(r_{ik}) P_l(\theta_{ijk}), \quad (3)$$

where  $n$  and  $l$  represent the orders of radial and angular expansions, respectively. Here, the summation runs over all neighbors of atom  $i$  within a certain cutoff distance,  $r_{ij}$  represents the distance between atoms  $i$  and  $j$ ,  $\theta_{ijk}$  is the angle for the triplet  $(ijk)$  with  $i$  being the central atom, and  $P_l(x)$  is the Legendre polynomial of order  $l$ . The functions  $g_n(r_{ij})$  depend solely on the distance  $r_{ij}$  and are therefore referred to as radial functions. These radial functions are defined as a linear combination of a number of basis functions:

$$g_n(r_{ij}) = \sum_k c_{nk}^{IJ} f_k(r_{ij}). \quad (4)$$

The basis functions  $f_k$  are constructed based on Chebyshev polynomials and a cutoff function, ensuring both formal completeness and smoothness. Explicit expressions for these functions can be found in Ref. 18. The expansion coefficients  $c_{nk}^{IJ}$  depend on  $n$  and  $k$  and also on the types (denoted as capitals  $I$  and  $J$ ) of atoms  $i$  and  $j$ . Due to the summation over neighbors, the descriptor components defined above are invariant with respect to permutation of atoms of the same type. More importantly, these coefficients are treated as trainable parameters [17], which is crucial for efficiently differentiating different atom pairs contributing to the descriptor.

While the descriptor parameters  $\{\mathbf{c}^{IJ}\}$  depend on the atom types (species), the NN parameters  $\mathbf{w}$  in NEP3 are the same for all the atom types. Therefore, as the number of atom types increases, the regression capacity of the NN model for each atom type decreases. To keep a constant

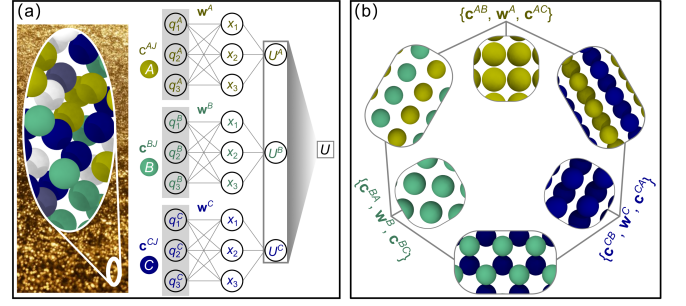


FIG. 1. (a) Schematic illustration of the architecture of the NEP4 model with distinct sets of NN parameters for different atom types. For a central atom of type  $A$ , the descriptor involves the  $\mathbf{c}^{AJ}$  parameters ( $J$  can be of any type), and the weight and bias parameters  $\mathbf{w}^A$  are specific for type  $A$ . Similar rules apply to central atoms of other types. The total energy  $U$  is the sum of the site energies for all the atoms in a given structure. By contrast, in NEP3 all atom types share a common set of NN parameters  $\mathbf{w}$ , which restricts the regression capacity. (b) Schematic illustration of the multi-loss evolutionary training algorithm. For a 3-component system, the optimization of the parameters related to atom type  $A$  (including  $\mathbf{w}^A$ ,  $\mathbf{c}^{AB}$ , and  $\mathbf{c}^{AC}$ ) is only driven by a loss function defined using the structures with the chemical compositions of  $A$ ,  $AB$ , and  $AC$ . In the conventional evolutionary algorithm, which is used in NEP3, a single loss function is used to optimize all parameters, which is less effective for training general-purpose models for many-component systems.

regression capacity per atom type, in the present work, we employ different sets of NN parameters  $\mathbf{w}^I$  for each atom type  $I$ . While this increases the total number of trainable parameters, it *does not* significantly increase the computational cost during MD simulations with the trained model, because it only involves a selection of the correct set of NN parameters for a given atom. With the extension, the site energy can be expressed as

$$U^i = \mathcal{N}(\mathbf{w}^I; \mathbf{q}^i(\{\mathbf{c}^{IJ}\})), \quad (5)$$

which constitutes the NEP4 model introduced in this paper (Fig. 1a).

**A multiple-loss evolutionary training algorithm for many-component systems.** While the increase in the number of trainable parameters does not significantly affect the inference speed, it does increase the number of iterations for training. It turns out that the training algorithm must be modified to achieve better performance for many-element systems. For training NEP models we use the separable natural evolution strategy (SNES) approach [27], which is a powerful black-box optimization algorithm that is particularly suitable for problems with many possible solutions [28]. It maintains a mean value and a variance for each trainable parameter that are updated according to the rank of a population of solutions. The rank is determined according to the loss function

to be minimized. The loss function  $L$  is constructed using calculated and reference data for energies, forces, and virials, and is a function of the trainable parameters, i.e.,

$$L = L(\{\mathbf{w}^I\}; \{\mathbf{c}^{IJ}\}). \quad (6)$$

The rank (or “fitness”) is of crucial importance in evolutionary algorithms, as it determines the relative weight of a solution in the population. However, using a single loss function can lead to ambiguity in rank assignment: Even if the total loss of solution X is smaller than that of solution Y, it does not guarantee that solution X is more accurate for all the subsystems in a many-element system. For example, solution X might offer higher accuracy for Au systems but lower accuracy for Ag systems. To account for this observation we define multiple loss functions for many-element systems. Since we are concerned with alloys, we cannot define a set of loss functions that have no common terms at all, but we can make a definition that minimizes the common parts. Naturally, we define the loss function for element  $I$  as the parts in Eq. (6) that are contributed by structures containing element  $I$ . For illustration, consider an explicit example with three elements, denoted  $A$ ,  $B$ , and  $C$ , respectively. The loss function for element  $A$  can be calculated by considering the chemical compositions  $A$ ,  $AB$ , and  $AC$  only, excluding  $B$ ,  $C$ , and  $BC$ . This loss function is used when training the parameters related to element  $A$ , which are  $\mathbf{w}^A$ ,  $\mathbf{c}^{AB}$ , and  $\mathbf{c}^{AC}$  (Fig. 1b). Using this multi-loss evolutionary algorithm, the training converges much faster than using a single-loss function. The efficiency improvement in training becomes more significant with an increasing number of elements, and is crucial for being able to develop models such as UNEP-v1.

**Construction of training data for many-component systems based on chemical generalizability.** The chemical space for 16 elements consists of  $2^{16} - 1 = 65\,535$  chemical combinations, including 16 unaries, 120 binaries, 560 ternaries, etc. It is formidable to construct a training dataset by enumerating all the possible chemical combinations. Fortunately, leveraging the construction of the radial functions in terms of linear combinations of basis functions provides a solution. The descriptor values for a given configuration of  $n$ -component ( $n > 2$ ) systems fall within the range spanned by those of the 1-component and 2-component systems derived from the same configuration by element substitution. Given the interpolation capabilities of NN, a NEP model trained using 1-component and 2-component structures is expected to predict reasonably well the behavior of  $n$ -component ( $n > 2$ ) systems. Therefore, our training dataset focused only on unary and binary systems.

For each unary or binary system, we constructed an initial training dataset with a few hundred struc-

tures. These structures included small cells with position and/or cell perturbations, cells with one to a few vacancies, cells with surfaces and various defects (such as grain boundaries) taken from the Materials Project [29] and the Open Quantum Materials Database [30], cells sampled from MD simulations based on an EAM potential [31] at various temperature (up to 5000 K) and pressure conditions including highly deformed structures (see Methods for details). There are about 60 000 structures in total for the 16 metals and their binary alloys. In spite of its seemingly modest size, this training dataset is remarkably diverse in the configuration space. Reference data (energy, force, and virial) for the structures were generated via DFT calculations using the VASP package (see Methods for details).

The diversity of the initial training dataset ensured a robust initial NEP model that could be used to run MD simulations at various thermodynamic conditions. From diverse MD trajectories generated by the initial NEP model, structures (still unary and binary only) were sampled and labeled using DFT calculations. Those with relatively large errors (NEP versus DFT) were identified and incorporated into the training set. This iterative process was repeated a few times until no large errors could be detected. This active-learning scheme, while simple, proved to be highly effective. The final training dataset contains 71 902 structures and 5 200 861 atoms in total. The DFT calculations for these structures required about five million CPU hours.

**Training and testing results.** Using the refined training dataset, we trained a NEP model (see Method for details on the hyperparameters) using the NEP4 approach as described above. We refer to this NEP model as UNEP-v1, which represents the first attempt at constructing a unified NEP model for many elements.

The parity plots for energy, force, and stress affirm the high accuracy of this UNEP-v1 model (Fig. 2a-c). Despite the large ranges of the three quantities, their root-mean-square errors (RMSEs) are relatively small, at 13.6 meV/atom, 167 meV/Å, and 0.98 GPa, respectively.

To validate our UNEP-v1 model we consider here three public datasets. Although the public datasets were not computed using exactly the same DFT settings as used for generating the UNEP-v1 training data, the resulting differences in force values are marginal (of the order of a few meV/Å) and are much smaller than the force RMSE achieved by UNEP-v1 (Fig. 2c). The comparison moreover shows that the UNEP-v1 model trained against 1-component and 2-component structures also performs very well for 3-component [34], 4-component [33], and 13-component [32] structures extracted from the datasets in the previous studies [32–34]. The testing RMSEs of the UNEP-v1 model for these three datasets are respectively 57 meV/Å, 196 meV/Å, and 258 meV/Å, which are com-



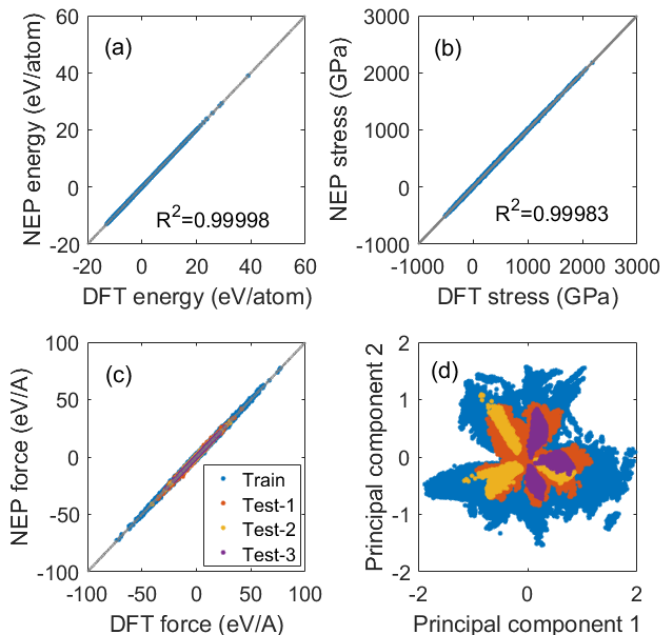


FIG. 2. (a-c) Parity plots for energy, stress, and force comparing DFT reference data and NEP predictions for the whole training dataset. In (c), there are three test sets containing  $n$ -component ( $n \geq 3$ ) structures, including one up to 13 components (Ag, Au, Cr, Cu, Mo, Ni, Pd, Pt, Ta, Ti, V, W, Zr) taken from Lopanitsyna *et al.* [32] (labeled Test-1), one up to 4 components (W, V, Ta, Mo) from Byggmästar *et al.* [33] (labeled Test-2), and one up to 3 components (Cu, Pd, Ni) from Zhao *et al.* [34] (labeled Test-3). (d) Distribution of the training and test structures shown in (c) in the 2D principal component space of the descriptor.

parable to those reported as training RMSEs in the original publications [32–34].

As a further test, we trained a NEP model by including relevant  $n$ -component ( $n \geq 3$ ) structures from the Open Quantum Materials Database database [30]. The RMSEs for the three public datasets obtained using this NEP model are only marginally improved compared to UNEP-v1, which demonstrates that our training dataset with  $n$ -component ( $n \leq 2$ ) structures is already sufficient for training a general-purpose NEP model for all the considered elements and their alloys.

As mentioned earlier, our approach to training data generation relies on the chemical generalizability embedded in the radial functions Eq. (4). This feature is illustrated by a principal component analysis of the descriptor space (Fig. 2d), which shows that the various  $n$ -component ( $n \geq 3$ ) structures fall comfortably within the space spanned by the 1-component and 2-component training structures.

## Evaluation of basic physical properties for the 16

**metal elements.** After having confirmed the high training accuracy of the UNEP-v1 model for 1-component and 2-component systems, and its high testing accuracy for systems with multiple components, we conducted an extensive evaluation of the UNEP-v1 model beyond RMSEs, focusing on various physical properties (see Methods for details on the calculations). Elastic constants, surface formation energies, mono-vacancy formation energies, melting point, and phonon dispersion relations were calculated for all 16 elements, using both the UNEP-v1 model and an EAM potential [31]. Detailed results for phonon dispersion relations are presented in Fig. S1, Fig. S2, and Fig. S3, while other physical properties are listed in Table S1, Table S2, Table S3, and Table S4. Fig. 3a-d show the parity plots comparing predictions of various basic properties from EAM and UNEP-v1 against DFT or experimental values. The EAM predictions have some outliers, especially concerning surface formation energy, while the UNEP-v1 predictions do not show any noticeable discrepancies.

The mean absolute errors for all the evaluated quantities calculated by averaging the absolute error between predicted (EAM or UNEP-v1) values and reference (DFT or experimental) values over all 16 elements are presented in Fig. 3e. UNEP-v1 consistently outperforms the EAM potential for all physical properties, and demonstrates a significant advantage in predicting surface formation energies, elastic constants, and vacancy formation energies.

We have additionally trained an ensemble of five NEP models using  $K$ -fold cross validation with  $K = 5$ , and compared the predictions for bulk and shear moduli as well as volume-per-atom for the ensemble to DFT reference data to estimate the uncertainty in the model predictions (Fig. 4a-c). Generally, the deviations in the predictions across the ensemble are very small, and agree well with the reference data. As a further illustration, we estimated the uncertainty in the phonon dispersion for Ag (Fig. 4d), illustrating the very small uncertainty throughout the entire Brillouin zone.

**Computational performance.** The computational efficiency of a MLP is crucial for its effective applications in large-scale MD simulations. Here, the UNEP-v1 model as implemented in GPUMD exhibits excellent computational performance (Table I). Using a single Nvidia A100 GPU, UNEP-v1 can reach a simulation size of about 14 million atoms and a computational speed of  $2.4 \times 10^7$  atom step/s, which is only a few times lower than that for the EAM potential ( $11 \times 10^7$  atom step/s) as implemented in LAMMPS [35] using the same hardware. To reach even larger simulation sizes, we implemented a multi-GPU version for UNEP-v1 that can effectively use the computational power of all the GPUs available on a computational node. With only 8 A100 GPUs, we

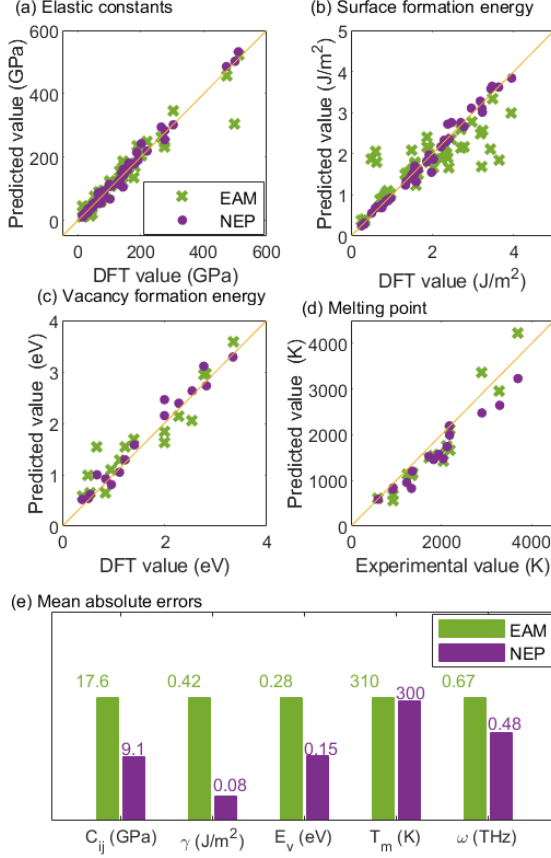


FIG. 3. (a-d) Elastic constants  $C_{ij}$ , formation energies for  $\{111\}$ ,  $\{110\}$ , and  $\{100\}$  surfaces  $\gamma$ , mono-vacancy formation energies  $E_v$  as well as melting points  $T_m$  as predicted by the EAM potential [31] and the UNEP-v1 model compared to DFT or experimental values for the 16 elements. (e) Mean absolute errors for the above four quantities as well as the phonon frequency  $\omega$  for EAM and UNEP-v1 against reference values.

can reach a simulation size of 100 million atoms, achieving much higher computational efficiency than either the deep potential (DP) (thousands of Nvidia V100 GPUs) [36, 37] or Allegro (128 A100 GPUs) approaches [38].

With 8 A100 GPUs, the overall computational speed of UNEP-v1 is about  $1.5 \times 10^8$  atom step/s. The parallel efficiency for UNEP-v1 with 8 A100 GPUs is 80%, while it is only about 50% for EAM with 4 A100 GPUs. The speed per GPU achieved by UNEP-v1 is significantly higher than those for the DP [36, 37] and Allegro approaches [38]. The excellent computational speed of UNEP-v1 allows us to tackle challenging problems in multi-principal-element alloys (MPEAs) as discussed below.

### Application to plasticity of multi-principal ele-

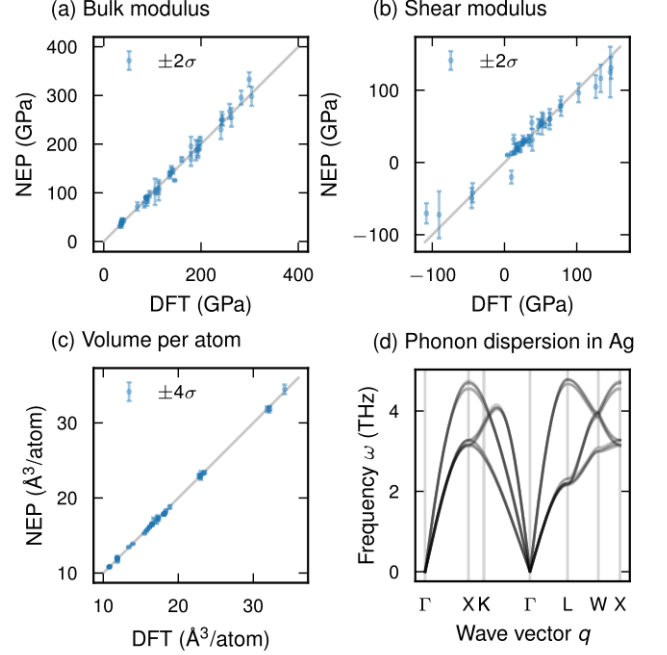


FIG. 4. (a-c) Parity plots for NEP model versus DFT data for bulk modulus, shear modulus, and volume per atom for the 16 elements, with error bars computed as the standard deviation in the predicted properties over an ensemble of five NEP models. The error bars correspond to  $2\sigma$  in the case of (a-b) and  $4\sigma$  for (c). The structures and reference DFT data were taken from the Materials Project [29]. (d) Phonon dispersion relations for Ag calculated using each model in the ensemble.

**ment alloys.** Refractory MPEAs have emerged as high-temperature materials, crystallizing typically in the body-centered cubic (BCC) solid solution phase. These alloys exhibit exceptional properties such as high ductility and mechanical strength at ultra-high temperature [39–42] as well as impressive irradiation resistance [43, 44]. However, their ductility at room temperature is limited [45, 46]. Recent experimental observations in alloys such as HfNbTaTiZr have revealed the presence of numerous straight screw dislocations and a substantial amount of dislocation debris [46, 47], consistent with known behavior in BCC metals [48]. Recent MD simulations have also indicated the possible crucial role of dislocation in the plastic flow of MPEAs [49–51]. Despite these insights, the complex structural and mechanical properties of MPEAs remain incompletely understood. Here, atomistic simulations employing accurate and efficient MLPs can provide further insights into the intricate behavior of these materials. Although there are a few available MLPs limited to specific alloys [49–51], a comprehensive general-purpose potential model capa-

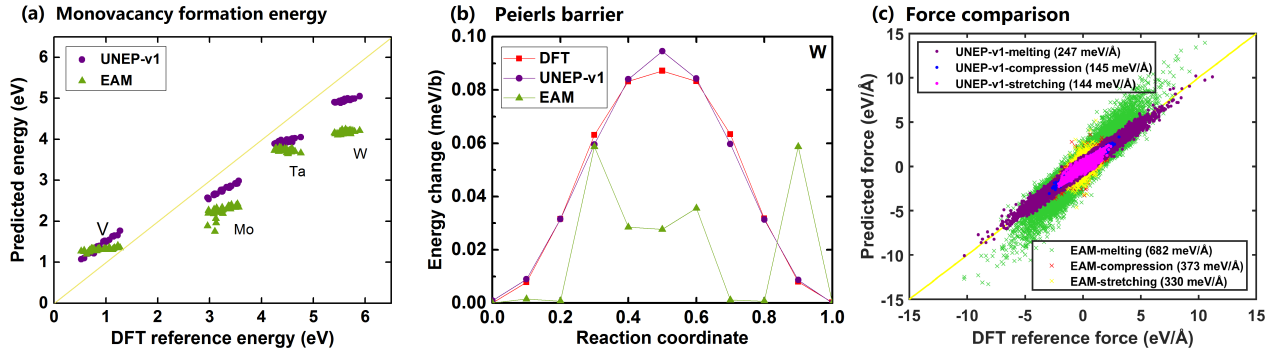


FIG. 5. (a) Mono-vacancy formation energy from UNEP-v1 and EAM compared to DFT data for an equimolar MoTaVW alloy with 128 atoms sampled from MC-MD simulations. (b) Peierls barrier for  $1/2\langle 111 \rangle$  screw dislocation migration in elemental W (see Fig. S4 for the other three species). (c) Comparisons of UNEP-v1, EAM, and DFT results for equimolar MoTaVW alloys sampled from various MD simulations using 256-atom supercells, including a melting process from 10 to 5000 K during 10 ns and deformation processes up to 25% compression and stretching at 300 K.

TABLE I. Computational performance of UNEP-v1 in comparison with DP [36, 37], Allegro [38], and EAM (using the GPU package of LAMMPS [35]) for large-scale MD simulations of typical metals. The speed is given in units of  $1 \times 10^4$  atom step/s/GPU. The DP results were obtained on V100 GPUs. All other data were generated using A100 GPUs, which offer approximately twice the computational performance of a V100 GPU.

Model-Element	# atoms	# GPUs	Speed
DP-Cu [36]	$127 \times 10^6$	27 300	4.5
DP-Cu [37]	$3400 \times 10^6$	27 300	33
Allegro-Ag [38]	$100 \times 10^6$	128	260
EAM-Cu	$23 \times 10^6$	1	11 000
EAM-Cu	$100 \times 10^6$	4	4930
UNEP-v1-Cu	$14 \times 10^6$	1	2350
UNEP-v1-Cu	$100 \times 10^6$	8	1880
UNEP-v1-Ag	$100 \times 10^6$	8	1720

ble of encompassing a wide range of elements and their alloys, providing both high efficiency and accuracy and enabling large-scale (up to millions of atoms) MD simulations of BCC MPEAs, is still lacking.

In this study, our UNEP-v1 model emerges as a promising solution, enabling large-scale MD simulations of MPEAs with superior accuracy and efficiency. To demonstrate its effectiveness in this context, we investigated the mechanism of plastic deformation of a MoTaVW alloy under compression. Our evaluation of the UNEP-v1 model involved comprehensive tests, including checking the vacancy formation energies (Fig. 5a) in equimolar MoTaVW alloys, Peierls barriers for the  $1/2\langle 111 \rangle$  screw dislocation (Fig. 5b) in elemental systems, and atomic forces in melting, compressive and tensile processes of equimolar MoTaVW alloys (Fig. 5c). The results illustrate the superior performance of UNEP-v1 compared to EAM potentials and its reliability for

studying structural and mechanical properties in large-scale MD simulations.

After having confirmed the accuracy, efficiency and reliability of our NEP model, we modeled an equimolar BCC polycrystalline MoTaVW system containing 100 205 176 atoms and conducted MD simulations to investigate changes in dislocation density under compression. These simulations involved compressive deformation at a strain rate of  $4.2 \times 10^8$ /s (see Methods for simulation details). The dislocation density decreases during the elastic stage, reaches a minimum at the yield strain  $\epsilon = 6\%$ , and gradually returns to the original level due to enhanced densification (Fig. 6a). The dislocation density plateaus for large strains ( $\epsilon \geq 16\%$ ), consistent with the behavior observed in BCC Ta [52]. It is noteworthy that stress-strain response and dislocation density exhibit contrasting trends under compression.

To gain deeper insight into the plastic deformation mechanisms, we extracted the distribution of dislocation density in snapshots of the polycrystalline MoTaVW system at selected strains (Fig. 6b-e). Notably, all dislocations are confined to grain boundaries of the polycrystalline system under compression, and this pattern remains unchanged throughout the linear response (“elastic”) region of the stress-strain curve (Fig. 6b-c). It is worth noting that dislocations transform from other types (labeled 1 and 2 in Fig. 6b) to  $1/2\langle 111 \rangle$  ones (Fig. 6c) in the elastic region (0–2.5%), and recover back at the yield strain of 6% (Fig. 6d). Subsequently, during the plastic stage (Fig. 6d-e), some of the grain boundaries begin to emit, slip, and pin dislocations into the grains along with boundary movement. This finding demonstrates the significant impacts of boundary stability on the hardness of MPEAs, as previously observed in the study of a NiMo alloy [53].

The application of our UNEP-v1 model to the plasticity of MPEAs, exemplified by MoTaVW alloy, is an im-

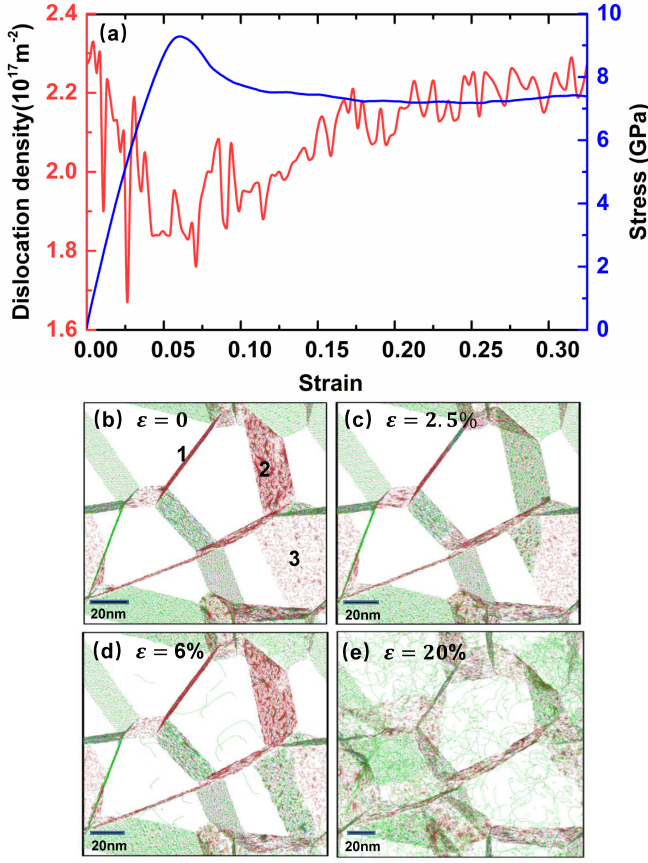


FIG. 6. Dislocation density as a function of compressive strain for equimolar polycrystalline MoTaVW alloys containing 12 grains with 100 million atoms at 300 K. (a) Strain-induced dislocation density and stress. (b-e) Distributions of dislocation in 20 nm thick slices at strains of (b)  $\epsilon = 0\%$ , (c)  $\epsilon = 2.5\%$ , (d)  $\epsilon = 6\%$ , and (e)  $\epsilon = 20\%$ , respectively. Grain boundaries are labeled by numbers for reference. The compressed direction is perpendicular to the plane of view. The  $1/2\langle 111 \rangle$  dislocations are depicted in green, while other dislocations are shown in red.

portant demonstration for the generality and high computational efficiency of our approach. Through 100-million-atom large-scale MD simulations, we have illuminated the intricate details of plastic deformation, shedding light on dislocation behavior in grain boundaries.

**Application to primary radiation damage in MPEAs.** Next, we demonstrate the versatility of the UNEP-v1 model through large-scale MD simulations of primary radiation damage in MPEAs, using again the MoTaVW alloy system for illustration (see Methods for details). Notably, these simulations set a new benchmark with a record-breaking size of 16 million atoms for MLPs in this specific type of simulations. Here, in order to accurately describe interactions at extremely short distances where large forces are at play, we incorporated a two-body Ziegler-Biersack-Littmark (ZBL) potential [54].

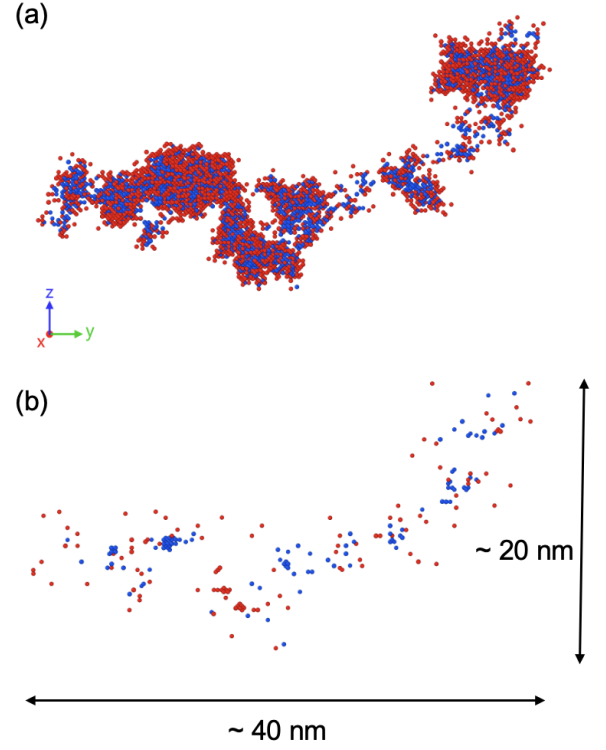


FIG. 7. Defect snapshots of a cascade in a MoTaVW alloy at (a) the peak damage state (at about 0.6 ps) and (b) the final damage state (at 140 ps). The red and blue dots represent interstitial atoms and vacancies, respectively.

Fig. 7a shows the defect snapshot of the peak-damage state formed at about 0.6 ps with a primary knock-on atom energy of 100 keV. The defect distribution stabilizes after a few tens of ps. Fig. 7b shows the stable defect distribution at 140 ps, revealing 121 residual point defects, including vacancies and interstitial atoms. The maximum cluster sizes for vacancies and interstitials are 15 and 11, respectively. In comparison, a previous study [55] on *elemental* W at similar simulation conditions reported 183 residual point defects with a maximum defect-cluster size exceeding 200 atoms. The MPEA thus features fewer defects and smaller defect clusters. Our simulation results are consistent with the experimental study of a similar tungsten-based refractory MPEA, which exhibits exceptional radiation resistance, negligible radiation hardening, and no evidence of radiation-induced dislocation loops even at a high dose level [43].

The enhanced radiation resistance of the tungsten-based refractory MPEAs could be attributed to the increased chemical complexity, leading to cascade splitting, as depicted in Fig. 7a. Cascade splitting results in the formation of smaller defect clusters and a more dispersed distribution of isolated (non-clustered) point defects. This specific application of our UNEP-v1 model to study primary radiation damage, through extensive MD



simulations involving 16 million atoms, provides further evidence for the generality and high efficiency of our approach. However, more detailed investigations are necessary to comprehensively characterize and understand the role of alloying in influencing radiation resistance.

## DISCUSSION

In summary, we have developed an advanced NEP approach capable of constructing accurate and efficient general-purpose MLPs for numerous elements and their alloys. Two crucial extensions have been made compared to previous NEP versions. Firstly, we employed distinct NNs for each species, ensuring consistent regression capacity even as the number of species grows. Secondly, we introduced multiple loss functions to optimize different subsets of the parameters, crucially accelerating the training process when using evolutionary algorithms with a large number of trainable parameters. We expect that this concept can boost more generally the application of evolutionary algorithms in solving complex optimization problems.

A pivotal insight driving the success of this approach is the recognition that chemical (species) information can be embedded in the trainable expansion coefficients of radial functions, dependent only on atom pairs and basis functions. As a result, the 1-component and 2-component structures delineate an outer boundary in descriptor space, while  $n$ -component structures with  $n \geq 3$  represent interpolation points in this space. Leveraging the exceptional interpolation capabilities of NNs, a NEP model trained solely with 1-component and 2-component structures performs very effectively for  $n$ -component structures with  $n \geq 3$ , provided the configuration space has been sufficiently explored.

While the current study focuses on 16 elements, our approach is scalable and adaptable for constructing NEP models across the entire periodic table. The primary challenge resides in the generation of the reference data, typically via DFT calculations, rather than the regression capabilities of the NEP model. Notably, our approach is also sustainable. Starting from our existing training set for 16 elements, one merely needs to include structures involving 17 chemical compositions (one 1-component and 16 2-component systems) to form a comprehensive training set for 17 elements. This method is far more economical than building an entirely new training set from scratch. Beyond extending the chemical space, one can also broaden the configuration space for existing chemical compositions, through established active-learning approaches, especially with the aid of structure searching methods [56].

The successful applications of UNEP-v1 model in studying plasticity and primary radiation damage in the MoTaVW refractory MPEAs demonstrate the versatility

and robustness of the NEP4 approach in general and the UNEP-v1 model in particular, establishing its significant potential for in-depth explorations and insights into the intricate behavior of complex materials such as MPEAs.

In conclusion, our study demonstrates the promise of our approach in constructing a unified general-purpose MLP for the periodic table with remarkable computational efficiency, taking full advantage of the embedded chemical generalizability, the outstanding interpolation capabilities of NNs and an advanced multiple-loss evolutionary training algorithm for multiple-component systems. By successfully developing a highly accurate and efficient MLP for a diverse range of elemental metals and alloys, our study showcases the versatility and applicability of our approach across various materials. These advancements mark a significant leap forward in enhancing the practical applications of MLPs in materials modeling, offering new opportunities for more accurate, efficient and even predictive computer simulations in materials science research.

## METHODS

**Molecular dynamics simulations for training structure generation.** To create the initial training structures, we used the LAMMPS package (23 Jun 2022) [35] to run MD simulations with cells ranging from 32 to 108 atoms. For each 1-component or 2-component system, we ran MD simulations in the isothermal-isobaric ensemble (zero target pressure) using the EAM potential [31] at 9 temperatures (50, 300, 800, 1300, 1700, 2300, 3000, 4000, and 5000 K), each for 2 ns. For each MD run, we sampled 5 structures. For each structure, we made three copies, one with a subsequent box scaling of 95%, one with 105%, and one with 5% (random) box perturbation. We also ran MD simulations at 300 K with tensile or compressing loading with a strain rate of  $2 \times 10^8$ /s for 1 to 2 ns and uniformly sampled 35 structures.

**DFT calculations for reference data generation.** After preparing the initial training structures, we performed quantum-mechanical calculations to obtain reference data, including the energy and virial for each structure and the force on each atom in each structure. DFT calculations as implemented in VASP [57] were performed to generate reference data. The INCAR file for VASP is presented in [Supplementary Note S1](#).

We used the projector augmented wave method [58, 59], the PBE functional [60], an energy cutoff of 600 eV, a  $\Gamma$ -centered  $k$ -point mesh with a spacing of  $0.2/\text{\AA}$ , and a threshold of  $1 \times 10^{-6}$  eV for the electronic self-consistent loop. We used the blocked Davidson iteration scheme for electronic minimization. The PREC tag in the VASP input file was set to **Accurate** to ensure accurate forces. A Gaussian smearing with a smearing width of 0.02 eV was

used. The Gaussian smearing is not the best choice for elemental metals and their alloys but we chose this in view of possible future extension of our approach to the whole periodic table. Our settings can ensure a convergence of the energy to 1 meV/atom for all the materials.

**The NEP training hyperparameters.** We used GPUMD v3.8 to train the UNEP-v1 model, which is a NEP4 model as introduced in this paper. The details of the `nep.in` input file we used can be found in [Supplementary Note S2](#).

The cutoff radii for radial and angular descriptor parts are 6 Å and 4 Å, respectively. For the radial descriptor components, we used 7 radial functions constructed from a linear combination of 13 basis functions. For the angular descriptor components, we used 5 radial functions constructed from a linear combination of 9 basis functions. The descriptor vector for one element thus has  $7 + 5 \times 5 = 32$  components. There are 80 neurons used in the hidden layer and the NN architecture for each element can be written as 32-80-1, corresponding to 2720 trainable parameters. For each pair of elements, there are  $7 \times 13 + 5 \times 9 = 136$  trainable descriptor parameters. The total number of trainable parameters in the UNEP-v1 model for 16 elements is thus  $2720 \times 16 + 136 \times 16^2 + 1 = 78\,337$ , where a global bias (shifting) parameter is included. The training was performed with a batch size of 5000 structures for 3 million generations (steps), which took about ten days using eight A100 GPUs.

**Calculations of basic physical properties.** To evaluate the reliability of the UNEP-v1 model in molecular statics and MD simulations, we calculated a set of relevant static and dynamic material properties, with a close comparison with EAM [31], DFT (if affordable), and experiments (if available). Energetics, elastic properties, and phonon dispersion relations were calculated with the help of GPUMD-WIZARD, ASE [61], PYNEP [18], CALORINE [18], and PHONOPY [62] packages. Melting points were calculated using the two-phase method as implemented in GPUMD [18] for UNEP-v1 and LAMMPS [35] for EAM, and are compared to experimental values [63]. Vacancy formation energies were evaluated using  $4 \times 5 \times 6$  supercells. The formation energies of free surfaces were evaluated with  $2 \times 2 \times 10$  supercells (taking a surface perpendicular to  $z$  as an example here). Training of the ensemble models with cross validation was performed using CALORINE. The uncertainties were estimated as the standard deviation in the predictions over the ensemble for the bulk and shear moduli and volume per atom.

**MD simulations for plasticity of MPEAs.** We used the UNEP-v1 model to drive MD calculations of the plasticity of MPEAs under compression using the

GPUMD package [18, 19]. First, we used the Voronoi algorithm implemented in ATOMSK [64] to build our initial MoTaVW polycrystalline MPEA model by removing overlapping atoms at boundaries. The model is composed of 12 grains with sizes ranging from 96 nm<sup>3</sup> to 195 nm<sup>3</sup>, and contains 100 205 176 atoms which randomly occupy a BCC lattice at equimolar ratios. The initial MoTaVW model was further relaxed by MD simulations for 500 ps in the isothermal-isobaric ensemble at 300 K and 0 GPa using the Bernetti-Bussi barostat [65] and Bussi-Donadio-Parrinello thermostat [66]. Finally we simulated uniaxial compressive deformation with a constant engineering strain rate of  $4.2 \times 10^8$ /s. The time step was kept fixed at 1 fs. The 2D visualization of dislocations perpendicular to the compressive axis was rendered using the OVITO package [67].

### MD simulations for primary radiation damage.

The MD simulations of the displacement cascade in MoTaVW were performed using the GPUMD package [18, 19] with the UNEP-v1 model and a repulsive two-body ZBL-like potential [54]. A periodic cubic simulation cell with 16 000 000 atoms was constructed by creating a random mixture of the Mo, Ta, V, and W atoms with equimolar ratio in a BCC crystal. We equilibrated this system in the isothermal-isobaric ensemble for 30 ps, with a target temperature of 300 K and a target pressure of 0 GPa. A primary knock-on atom with an energy of 100 keV moving in the high-index direction  $\langle 135 \rangle$  (to avoid channeling effects) was then created at the center of the simulation cell. Atoms within a thickness of three lattice constants of the boundaries were maintained at 300 K. The integration time step had an upper limit of 1 fs and was dynamically determined so that the fastest atom could move at most 0.015 Å (less than 0.5% of the lattice constant) within one step. The total number of steps is 200 000, corresponding to 140 ps. Electronic stopping [68] was applied as a frictional force on atoms with a kinetic energy over 10 eV. We used the OVITO package [67] for defect analysis and visualization. The interstitials and vacancies were identified by using the Wigner-Seitz cell method. The defects were grouped into clusters: two vacancies were considered to be in the same cluster if the distance between them was within the second-nearest-neighbor distance, while the third-nearest-neighbor distance was used to identify self-interstitial clusters.

### DATA AVAILABILITY

The training data and trained NEP models are freely available at the Zenodo repository <https://doi.org/10.5281/zenodo.10081677>. The high-throughput-calculation inputs/outputs for the basic physical prop-

erties are freely available at <https://github.com/Jonsnow-willow/GPUMD-Wizard>.

### CODE AVAILABILITY

The source code and documentation for CALORINE are available at <https://gitlab.com/materials-modeling/calorine> and <https://calorine.materialsmodeling.org/>, respectively. The source code and documentation for GPUMD are available at <https://github.com/brucefan1983/GPUMD> and <https://gpumd.org>, respectively. The source code and documentation for GPUMD-WIZARD are available at <https://github.com/Jonsnow-willow/GPUMD-Wizard>. The source code and documentation for PYNEP are available at <https://github.com/bigd4/PyNEP> and <https://pynep.readthedocs.io/en/latest/>, respectively.

### DECLARATION OF COMPETING INTEREST

The authors declare that they have no competing interests.

### CONTRIBUTIONS

Keke Song, Rui Zhao, Yanzhou Wang, and Nan Xu prepared the training and test structures. Keke Song, Yanzhou Wang, Zhiqiang Zhao, Ting Liang, Jiuyang Shi, Junjie Wang, Ke Xu, Shuang Lyu, Zezhu Zeng, and Shirong Liang performed the DFT calculations. Keke Song, Shunda Chen, and Yanzhou Wang tested the various hyperparameters and trained the NEP models. Penghua Ying analyzed the descriptor space. Keke Song, Rui Zhao, Jiahui Liu, Ke Xu, Ting Liang, Zhiqiang Zhao, and Haikuan Dong evaluated the basic physical properties. Eric Lindgren trained and analyzed the ensemble models. Yong Wang and Shunda Chen evaluated the computational performance. Jiahui Liu performed the radiation damage simulations. Zheyong Fan and Shunda Chen developed the NEP4 model and the multiple-loss evolutionary training algorithm. Ligang Sun, Yue Chen, Zhuhua Zhang, Wanlin Guo, Ping Qian, Jian Sun, Paul Erhart, Tapio Ala-Nissila, Yanjing Su, and Zheyong Fan supervised the project.

### ACKNOWLEDGEMENTS

Keke Song, Jiahui Liu, Yanzhou Wang, Ping Qian, and Yanjing Su acknowledge support from the National Key R & D Program of China (No. 2022YFB3707500) and the National Natural Science Foundation of China (NSFC)

(No. 92270001). Yanzhou Wang and Tapio Ala-Nissila have been supported in part by the Academy of Finland through its Quantum Technology Finland CoE grant No. 312298. Eric Lindgren and Paul Erhart acknowledge funding from the Swedish Research Council (Nos. 2020-04935 and 2021-05072) and the Swedish Foundation for Strategic Research via the SwedNESS graduate school (GSn15-0008) as well as computational resources provided by the National Academic Infrastructure for Supercomputing in Sweden at NSC and C3SE partially funded by the Swedish Research Council through grant agreement No. 2022-06725. Yong Wang, Jiuyang Shi, Junjie Wang, and Jian Sun acknowledge support from NSFC (Nos. 12125404, 11974162, and 11834006) and the Fundamental Research Funds for the Central Universities, and computational sources from the High Performance Computing Center of Collaborative Innovation Center of Advanced Microstructures and the high-performance supercomputing center of Nanjing University. Ke Xu and Ting Liang acknowledge support from the National Key R&D Project from Ministry of Science and Technology of China (No. 2022YFA1203100), the Research Grants Council of Hong Kong (No. AoE/P-701/20), and RGC GRF (No. 14220022). Zhiqiang Zhao, Zhuhua Zhang, and Wanlin Guo acknowledge support from the NSFC Projects of International Cooperation and Exchanges (No. 12261160367). Zezhu Zeng, Shuang Lyu, and Yue Chen are grateful for the research computing facilities offered by ITS, HKU.

---

\* These authors contributed equally to this work.

† [jiansun@nju.edu.cn](mailto:jiansun@nju.edu.cn)

‡ [erhart@chalmers.se](mailto:erhart@chalmers.se)

§ [yjsu@ustb.edu.cn](mailto:yjsu@ustb.edu.cn)

¶ [brucenju@gmail.com](mailto:brucenju@gmail.com)

- [1] M. S. Daw and M. I. Baskes, Embedded-atom method: Derivation and application to impurities, surfaces, and other defects in metals, *Phys. Rev. B* **29**, 6443 (1984).
- [2] M. W. Finnis and J. E. Sinclair, A simple empirical n-body potential for transition metals, *Philosophical Magazine A* **50**, 45 (1984).
- [3] J. Behler, Perspective: Machine learning potentials for atomistic simulations, *The Journal of Chemical Physics* **145**, 170901 (2016).
- [4] V. L. Deringer, M. A. Caro, and G. Csányi, Machine Learning Interatomic Potentials as Emerging Tools for Materials Science, *Advanced Materials* **31**, 1902765 (2019).
- [5] T. Mueller, A. Hernandez, and C. Wang, Machine learning for interatomic potential models, *The Journal of Chemical Physics* **152**, 050902 (2020).
- [6] F. Noé, A. Tkatchenko, K.-R. Müller, and C. Clementi, Machine Learning for Molecular Simulation, *Annual Review of Physical Chemistry* **71**, 361 (2020).
- [7] Y. Mishin, Machine-learning interatomic potentials for materials science, *Acta Materialia* **214**, 116980 (2021).

- [8] O. T. Unke, S. Chmiela, H. E. Sauceda, M. Gastegger, I. Poltavsky, K. T. Schütt, A. Tkatchenko, and K.-R. Müller, Machine Learning Force Fields, *Chemical Reviews* **121**, 10142 (2021).
- [9] A. V. Shapeev, Moment Tensor Potentials: A Class of Systematically Improvable Interatomic Potentials, *Multiscale Modeling & Simulation* **14**, 1153 (2016).
- [10] R. Drautz, Atomic cluster expansion for accurate and transferable interatomic potentials, *Phys. Rev. B* **99**, 014104 (2019).
- [11] A. Thompson, L. Swiler, C. Trott, S. Foiles, and G. Tucker, Spectral neighbor analysis method for automated generation of quantum-accurate interatomic potentials, *Journal of Computational Physics* **285**, 316 (2015).
- [12] J. Behler and M. Parrinello, Generalized Neural-Network Representation of High-Dimensional Potential-Energy Surfaces, *Phys. Rev. Lett.* **98**, 146401 (2007).
- [13] A. P. Bartók, M. C. Payne, R. Kondor, and G. Csányi, Gaussian Approximation Potentials: The Accuracy of Quantum Mechanics, without the Electrons, *Phys. Rev. Lett.* **104**, 136403 (2010).
- [14] S. Batzner, A. Musaelian, L. Sun, M. Geiger, J. P. Mailoa, M. Kornbluth, N. Molinari, T. E. Smidt, and B. Kozinsky, E(3)-equivariant graph neural networks for data-efficient and accurate interatomic potentials, *Nature communications* **13**, 2453 (2022).
- [15] I. Batatia, D. P. Kovacs, G. Simm, C. Ortner, and G. Csányi, MACE: Higher Order Equivariant Message Passing Neural Networks for Fast and Accurate Force Fields, in *Advances in Neural Information Processing Systems*, Vol. 35, edited by S. Koyejo, S. Mohamed, A. Agarwal, D. Belgrave, K. Cho, and A. Oh (Curran Associates, Inc., 2022) pp. 11423–11436.
- [16] Z. Fan, Z. Zeng, C. Zhang, Y. Wang, K. Song, H. Dong, Y. Chen, and T. Ala-Nissila, Neuroevolution machine learning potentials: Combining high accuracy and low cost in atomistic simulations and application to heat transport, *Phys. Rev. B* **104**, 104309 (2021).
- [17] Z. Fan, Improving the accuracy of the neuroevolution machine learning potential for multi-component systems, *Journal of Physics: Condensed Matter* **34**, 125902 (2022).
- [18] Z. Fan, Y. Wang, P. Ying, K. Song, J. Wang, Y. Wang, Z. Zeng, K. Xu, E. Lindgren, J. M. Rahm, A. J. Gabourie, J. Liu, H. Dong, J. Wu, Y. Chen, Z. Zhong, J. Sun, P. Erhart, Y. Su, and T. Ala-Nissila, Gpumd: A package for constructing accurate machine-learned potentials and performing highly efficient atomistic simulations, *The Journal of Chemical Physics* **157**, 114801 (2022).
- [19] Z. Fan, W. Chen, V. Vierimaa, and A. Harju, Efficient molecular dynamics simulations with many-body potentials on graphics processing units, *Computer Physics Communications* **218**, 10 (2017).
- [20] S. Takamoto, S. Izumi, and J. Li, Teanet: Universal neural network interatomic potential inspired by iterative electronic relaxations, *Computational Materials Science* **207**, 111280 (2022).
- [21] S. Takamoto, C. Shinagawa, D. Motoki, K. Nakago, W. Li, I. Kurata, T. Watanabe, Y. Yayama, H. Iriguchi, Y. Asano, *et al.*, Towards universal neural network potential for material discovery applicable to arbitrary combination of 45 elements, *Nature Communications* **13**, 1 (2022).
- [22] C. Chen and S. P. Ong, A universal graph deep learning interatomic potential for the periodic table, *Nature Computational Science* **2**, 718 (2022).
- [23] A. P. Bartók, J. Kermode, N. Bernstein, and G. Csányi, Machine Learning a General-Purpose Interatomic Potential for Silicon, *Phys. Rev. X* **8**, 041048 (2018).
- [24] P. Rowe, V. L. Deringer, P. Gasparotto, G. Csányi, and A. Michaelides, An accurate and transferable machine learning potential for carbon, *The Journal of Chemical Physics* **153**, 034702 (2020).
- [25] R. Jana and M. A. Caro, Searching for iron nanoparticles with a general-purpose Gaussian approximation potential, *Phys. Rev. B* **107**, 245421 (2023).
- [26] J. Kloppenburg, L. B. Pártay, H. Jónsson, and M. A. Caro, A general-purpose machine learning Pt interatomic potential for an accurate description of bulk, surfaces, and nanoparticles, *The Journal of chemical physics* **158**, 134704 (2023).
- [27] T. Schaul, T. Glasmachers, and J. Schmidhuber, High Dimensions and Heavy Tails for Natural Evolution Strategies, in *Proceedings of the 13th Annual Conference on Genetic and Evolutionary Computation*, GECCO '11 (Association for Computing Machinery, New York, NY, USA, 2011) pp. 845–852.
- [28] Daan Wierstra and Tom Schaul and Tobias Glasmachers and Yi Sun and Jan Peters and Jürgen Schmidhuber, Natural evolution strategies, *Journal of Machine Learning Research* **15**, 949 (2014).
- [29] A. Jain, S. P. Ong, G. Hautier, W. Chen, W. D. Richards, S. Dacek, S. Cholia, D. Gunter, D. Skinner, G. Ceder, and K. a. Persson, The Materials Project: A materials genome approach to accelerating materials innovation, *APL Materials* **1**, 011002 (2013).
- [30] S. Kirklin, J. E. Saal, B. Meredig, A. Thompson, J. W. Doak, M. Aykol, S. Rühl, and C. Wolverton, The Open Quantum Materials Database (OQMD): assessing the accuracy of DFT formation energies, *npj Computational Materials* **1**, 15010 (2015).
- [31] X. W. Zhou, R. A. Johnson, and H. N. G. Wadley, Misfit-energy-increasing dislocations in vapor-deposited CoFe/NiFe multilayers, *Phys. Rev. B* **69**, 144113 (2004).
- [32] N. Lopanitsyna, G. Fraux, M. A. Springer, S. De, and M. Ceriotti, Modeling high-entropy transition metal alloys with alchemical compression, *Phys. Rev. Mater.* **7**, 045802 (2023).
- [33] J. Byggmästar, K. Nordlund, and F. Djurabekova, Simple machine-learned interatomic potentials for complex alloys, *Phys. Rev. Mater.* **6**, 083801 (2022).
- [34] R. Zhao, S. Wang, Z. Kong, Y. Xu, K. Fu, P. Peng, and C. Wu, Development of a neuroevolution machine learning potential of Pd-Cu-Ni-P alloys, *Materials & Design* **231**, 112012 (2023).
- [35] A. P. Thompson, H. M. Aktulga, R. Berger, D. S. Bolinteanu, W. M. Brown, P. S. Crozier, P. J. in 't Veld, A. Kohlmeyer, S. G. Moore, T. D. Nguyen, R. Shan, M. J. Stevens, J. Tranchida, C. Trott, and S. J. Plimpton, LAMMPS - a flexible simulation tool for particle-based materials modeling at the atomic, meso, and continuum scales, *Computer Physics Communications* **271**, 108171 (2022).
- [36] W. Jia, H. Wang, M. Chen, D. Lu, L. Lin, R. Car, W. E, and L. Zhang, Pushing the Limit of Molecular Dynamics with Ab Initio Accuracy to 100 Million Atoms with Machine Learning, in *Proceedings of the International Con-*



- ference for High Performance Computing, Networking, Storage and Analysis, SC '20 (IEEE Press, 2020).
- [37] Z. Guo, D. Lu, Y. Yan, S. Hu, R. Liu, G. Tan, N. Sun, W. Jiang, L. Liu, Y. Chen, L. Zhang, M. Chen, H. Wang, and W. Jia, Extending the limit of molecular dynamics with ab initio accuracy to 10 billion atoms, in *Proceedings of the 27th ACM SIGPLAN Symposium on Principles and Practice of Parallel Programming*, PPoPP '22 (Association for Computing Machinery, New York, NY, USA, 2022) p. 205–218.
  - [38] A. Musaelian, S. Batzner, A. Johansson, L. Sun, C. J. Owen, M. Kornbluth, and B. Kozinsky, Learning local equivariant representations for large-scale atomistic dynamics, *Nature Communications* **14**, 579 (2023).
  - [39] O. Senkov, S. Gorsse, and D. Miracle, High temperature strength of refractory complex concentrated alloys, *Acta Materialia* **175**, 394 (2019).
  - [40] E. P. George, D. Raabe, and R. O. Ritchie, High-entropy alloys, *Nature Reviews Materials* **4**, 515 (2019).
  - [41] F. G. Coury, M. Kaufman, and A. J. Clarke, Solid-solution strengthening in refractory high entropy alloys, *Acta Materialia* **175**, 66 (2019).
  - [42] P. Shi, W. Ren, T. Zheng, Z. Ren, X. Hou, J. Peng, P. Hu, Y. Gao, Y. Zhong, and P. Liaw, Enhanced strength–ductility synergy in ultrafine-grained eutectic high-entropy alloys by inheriting microstructural lamellae, *Nature Communications* **10**, 489 (2019).
  - [43] O. El-Atwani, N. Li, M. Li, A. Devaraj, J. K. S. Baldwin, M. M. Schneider, D. Sobieraj, J. S. Wróbel, D. Nguyen-Manh, S. A. Maloy, and E. Martinez, Outstanding radiation resistance of tungsten-based high-entropy alloys, *Science Advances* **5**, eaav2002 (2019).
  - [44] O. El Atwani, H. T. Vo, M. A. Tunes, C. Lee, A. Alvarado, N. Krienke, J. D. Poplawsky, A. A. Kohnert, J. Gigax, W.-Y. Chen, M. Li, Y. Q. Wang, J. S. Wróbel, D. Nguyen-Manh, J. K. S. Baldwin, O. U. Tukac, E. Aydogan, S. Fensin, and E. Martinez, A quinary WTaCrVHf nanocrystalline refractory high-entropy alloy withholding extreme irradiation environments, *Nature Communications* **14** (2023).
  - [45] O. N. Senkov, D. B. Miracle, K. J. Chaput, and J.-P. Couzinié, Development and exploration of refractory high entropy alloys—a review, *Journal of Materials Research* **33**, 3092–3128 (2018).
  - [46] J.-P. Couzinié and G. Dirras, Body-centered cubic high-entropy alloys: From processing to underlying deformation mechanisms, *Materials Characterization* **147**, 533 (2019).
  - [47] L. Lilensten, J.-P. Couzinié, L. Perrière, A. Hocini, C. Keller, G. Dirras, and I. Guillot, Study of a bcc multi-principal element alloy: Tensile and simple shear properties and underlying deformation mechanisms, *Acta Materialia* **142**, 131 (2018).
  - [48] D. Caillard and J.-L. Martin, *Thermally activated mechanisms in crystal plasticity* (Elsevier, 2003).
  - [49] X.-G. Li, C. Chen, H. Zheng, Y. Zuo, and S. P. Ong, Complex strengthening mechanisms in the NbMoTaW multi-principal element alloy, *npj Computational Materials* **6**, 70 (2020).
  - [50] S. Yin, Y. Zuo, A. Abu-Odeh, H. Zheng, X.-G. Li, J. Ding, S. P. Ong, M. Asta, and R. O. Ritchie, Atomistic simulations of dislocation mobility in refractory high-entropy alloys and the effect of chemical short-range order, *Nature communications* **12**, 4873 (2021).
  - [51] H. Zheng, L. T. Fey, X.-G. Li, Y.-J. Hu, L. Qi, C. Chen, S. Xu, I. J. Beyerlein, and S. P. Ong, Multi-scale investigation of short-range order and dislocation glide in MoNbTi and TaNbTi multi-principal element alloys, *npj Computational Materials* **9**, 89 (2023).
  - [52] L. A. Zepeda-Ruiz, A. Stukowski, T. Oppelstrup, and V. V. Bulatov, Probing the limits of metal plasticity with molecular dynamics simulations, *Nature* **550**, 492 (2017).
  - [53] J. Hu, Y. Shi, X. Sauvage, G. Sha, and K. Lu, Grain boundary stability governs hardening and softening in extremely fine nanograined metals, *Science* **355**, 1292 (2017).
  - [54] J. F. Ziegler and J. P. Biersack, The stopping and range of ions in matter, in *Treatise on Heavy-Ion Science: Volume 6: Astrophysics, Chemistry, and Condensed Matter*, edited by D. A. Bromley (Springer US, Boston, MA, 1985) pp. 93–129.
  - [55] J. Liu, J. Byggmästar, Z. Fan, P. Qian, and Y. Su, Large-scale machine-learning molecular dynamics simulation of primary radiation damage in tungsten, *Phys. Rev. B* **108**, 054312 (2023).
  - [56] J. Wang, H. Gao, Y. Han, C. Ding, S. Pan, Y. Wang, Q. Jia, H.-T. Wang, D. Xing, and J. Sun, MAGUS: machine learning and graph theory assisted universal structure searcher, *National Science Review* **10**, nwad128 (2023).
  - [57] G. Kresse and J. Furthmüller, Efficient iterative schemes for ab initio total-energy calculations using a plane-wave basis set, *Phys. Rev. B* **54**, 11169 (1996).
  - [58] P. E. Blöchl, Projector augmented-wave method, *Phys. Rev. B* **50**, 17953 (1994).
  - [59] G. Kresse and D. Joubert, From ultrasoft pseudopotentials to the projector augmented-wave method, *Phys. Rev. B* **59**, 1758 (1999).
  - [60] J. P. Perdew, K. Burke, and M. Ernzerhof, Generalized Gradient Approximation Made Simple, *Phys. Rev. Lett.* **77**, 3865 (1996).
  - [61] A. H. Larsen, J. J. Mortensen, J. Blomqvist, I. E. Castelli, R. Christensen, M. Dulak, J. Friis, M. N. Groves, B. Hammer, C. Hargus, E. D. Hermes, P. C. Jennings, P. B. Jensen, J. Kermode, J. R. Kitchin, E. L. Kolsbjerg, J. Kubal, K. Kaasbjerg, S. Lysgaard, J. B. Maronsson, T. Maxson, T. Olsen, L. Pastewka, A. Peterson, C. Rostgaard, J. Schiøtz, O. Schütt, M. Strange, K. S. Thygesen, T. Vegge, L. Vilhelmsen, M. Walter, Z. Zeng, and K. W. Jacobsen, The atomic simulation environment—a Python library for working with atoms, *Journal of Physics: Condensed Matter* **29**, 273002 (2017).
  - [62] A. Togo, L. Chaput, T. Tadano, and I. Tanaka, Implementation strategies in phonopy and phono3py, *J. Phys. Condens. Matter* **35**, 353001 (2023).
  - [63] W. E. Haynes, *CRC handbook of chemistry and physics (97th ed.)* (CRC Press llc Boca Raton, FL, 2016).
  - [64] P. Hirel, AtomsK: A tool for manipulating and converting atomic data files, *Computer Physics Communications* **197**, 212 (2015).
  - [65] M. Bernetti and G. Bussi, Pressure control using stochastic cell rescaling, *The Journal of Chemical Physics* **153**, 10.1063/5.0020514 (2020).
  - [66] G. Bussi, D. Donadio, and M. Parrinello, Canonical sampling through velocity rescaling, *The Journal of chemical physics* **126**, 10.1063/1.2408420 (2007).
  - [67] A. Stukowski, Visualization and analysis of atomistic simulation data with ovito—the open visualization tool,

Modelling and Simulation in Materials Science and Engineering **18**, 015012 (2009).

- [68] K. Nordlund, Molecular dynamics simulation of ion ranges in the 1-100 keV energy range, [Computational](#)

[Materials Science](#) **3**, 448 (1995).